Impacts of Salinity and Consolidation on the Microstructure and Erosion Threshold of Cohesive Sediment

Jorge Emilio San Juan[1], Guanju Wei[2], and Qingjun Judy Yang[1]

[1]University of Minnesota
[2]University of Minnesota-Twin Cities

November 24, 2022

Abstract

The transport of cohesive sediment is known to be impacted by salinity and consolidation, which control the electro-chemical force and microscale structures of clay. However, such impacts remain poorly understood, due to a lack of direct visualization and characterization methods. Here, we combine a transparent clay, fluorescent dye, and laser-based technologies to directly visualize the transport of clay and its microstructure and identify the critical shear stress for clay erosion, Tau_crit. We show that as salinity increases, Tau_crit increases by over one order of magnitude under low salinity (<1.52 ppt) and then decreases under high salinity (>1.52 ppt). This non-monotonic dependence of Tau_crit on salinity can be attributed to a change in clay microstructures. In addition, we show an increase in Tau_crit after clay consolidation and attribute it to a change in clay microstructures. Our results demonstrate the important role of salinity, consolidation, clay microstructure, in controlling clay erosion.

Impacts of Salinity and Consolidation on the Microstructure and Erosion Threshold of Cohesive Sediment

Jorge E. San Juan[1], William G. Wei[1], and Judy Q. Yang[1]

[1] St. Anthony Falls Laboratory, Department of Civil, Environmental, and Geo-Engineering, University of Minnesota Twin Cities, MN, USA.

Corresponding author: Judy Q. Yang (judyyang@umn.edu)

Key Points:

- Water salinity alters the erosion threshold of a cohesive smectite clay by over one order of magnitude.
- The critical bed shear stress to erode clay first increases and then decreases with increasing water salinity.
- The non-monotonic dependency of the critical shear stress on salinity can be attributed to the change in clay microstructure.

Abstract

The transport of cohesive sediment is known to be impacted by salinity and consolidation, which control the electro-chemical force and microscale structures of clay. However, such impacts remain poorly understood, due to a lack of direct visualization and characterization methods. Here, we combine a transparent clay, fluorescent dye, and laser-based technologies to directly visualize the transport of clay and its microstructure and identify the critical shear stress for clay erosion, $\tau_{b,crit}$. We show that as salinity increases, $\tau_{b,crit}$ increases by over one order of magnitude under low salinity (<1.52 ppt) and then decreases under high salinity (>1.52 ppt). This non-monotonic dependence of $\tau_{b,crit}$ on salinity can be attributed to a change in clay microstructures. In addition, we show an increase in $\tau_{b,crit}$ after clay consolidation and attribute it to a change in clay microstructures. Our results demonstrate the important role of salinity, consolidation, clay microstructure, in controlling clay erosion.

Plain Language Summary

Cohesive sediment such as mud is ubiquitous in aquatic environments, such as rivers, coasts, and estuaries. Clay is a major component that contributes to the cohesiveness of sediment. Predicting the transport of clay is critical for predicting and controlling coastal and riverine erosion. Here, we directly visualize the erosion and microstructure of a fluorescently-labeled transparent clay and quantify the critical condition to erode clay. We find that the critical force per bed area for clay erosion varies by over one order of magnitude with varying salinity and by two times with varying consolidation time. We further find that such dependency of clay erosion on salinity and consolidation is related to the microscale structures of clay. Salinity alters the clay microstructure into either a gel-like network or a mixture of separated micro-size aggregates. When clay forms gel at low salinity, it becomes harder to erode than when it forms separated aggregates. Sediment consolidation makes the mixture more compact with time. When clay aggregates become more compact, it also becomes harder to erode. Our study highlights the importance of salinity, condensation, and clay microscale structures on clay erosion and will help improve predictions of coastal and riverine erosion.

1 Introduction

Accelerating erosion has become a major threat of coastal ecosystems (Winterwerp et al., 2013). Control and management of erosion rely on accurate physics-based predictions of sediment transport (Adam, 2019; Haight et al., 2019). Sediments in near-shore environments are predominantly cohesive due to the existence of 10-40% of fine clay particles in the sediment (De Jonge, 1988). Prediction of cohesive sediment transport remains challenging because such transport is impacted by many factors that are not represented in classic sediment transport equations (Partheniades, 1986; Berlamont et al., 1993; Grabowski et al., 2011; Forsberg et al., 2018), such as salinity and sediment consolidation (Lick and McNeil, 2001; Grabowski et al., 2011). Laboratory studies on natural cohesive sediment observed that a 1.5 ppt (parts-per-thousand) increase in water salinity can lead to 90% increase in the critical stress to erode cohesive sediment bed (Krone, 1962; Parchure and Mehta, 1985; Berlamont et al., 1993). In addition, other studies show that consolidation, or the compact of sediment on their own weight (Nicholson and O' Connor, 1986), reduces the rate of bed resuspension by increasing bed cohesive strength (Mehta, 1986). Understanding how salinity and consolidation impact the threshold of cohesive sediment transport is important because changes in water salinity and sediment consolidation can lead to large extensions of fringe erosion in salt marshes (Kennish, 2001, Pieterse et a., 2017). However, such understanding remains incomplete due to a lack of experimental tools to directly visualize the transport of opaque clay.

The goal of this study is to reveal the impacts of salinity and consolidation on the transport of smectite clay, which is common in coastal sediment (Winterwerp et al., 2013; Sartor et al., 2019). We hypothesize that salinity and consolidation control the transport of smectite clay by altering the microscopic interactions among, or microstructures of, clay particles. Microstructural chances take place because smectite clay can form gel (network-like structure), below a critical ionic strength or salinity, and form phase-separated individual micro-size aggregates above a critical ionic strength (Tanaka et al., 2004; Ruzicka and Zaccarelli, 2011). The gelatinous network structures of smectite have shown to resist higher shear strength than non-gelatinous smectite aggregates (Lick and McNeil, 2001; Hedstrom et al., 2016). Nevertheless, the impacts of salinity on clay microstructures and transport remain poorly understood and contradicting behavior have been reported. An increase in pore-water salinity has been found to decrease the clay strength (Lick and McNeil, 2001), which is contradictory to the observation that a decrease in salinity leads to weakening of bentonite gel which likely causes to decrease in clay strength (Hedstrom et al., 2016). In addition to clay salinity, consolidation can modify the clay microstructure and alter the erosion threshold (Winterwerp et al., 2013). Nonconsolidated fluid mud, at the limit of gel-point concentrations, show plastic behavior and shear thinning characteristics, while consolidated clays show pseudo plastic or viscoelastic characteristics (Guillou et al., 2011). Systematically controlled experiments are needed to reveal how salinity and consolidation affect clay microstructures and the threshold of clay transport.

We propose to directly measure the microstructure and erosion threshold of a transparent smectite clay, laponite, through fluorescence-based visualization. Laponite is a synthetic clay made from natural rock and has similar molecular structures as bentonite (Laponite-RD, BYK Additives and Instruments, 2013). The usage of transparent clay and fluorescence made it possible to overcome the technology limitations encountered in previous studies using opaque clay. Specifically, previous studies estimate erosion threshold for cohesive sediment by extrapolating zero-crossing values from erosion rate, estimated from bulk suspended sediment concentration, versus shear stress (e.g., Parchure and Mehta, 1985). The concentration of suspended sediment is usually indirectly measured based on acoustic techniques such as the backscattered acoustic signals (Pedocchi and García, 2012), which is insensitive to low concentration at the beginning of the erosion and does not consider the soil matrix or structures of the sediment particles (Yuan et al., 2022). To identify the initiation of bed erosion, a method to directly track the movement of the sediment surface is needed (e.g., Zhang and Yu, 2017). The synthetic and transparent laponite used in this study enables direct visualization of the movement of the sediment bed as well as the microstructures of clay aggregates.

In this study, we first identify the critical shear stress for clay erosion by tracking the movement of the surface of laponite bed under progressively increasing shear. Second, we reveal a non-monotonic relationship between the critical shear stress and water salinity. We demonstrate that such non-monotonic relationship is related to the gelation state, or microstructure, of laponite which is controlled by salinity (e.g., Thompson and Butterworth, 1992; Tanaka et al., 2004; Mongondry et al., 2005; Huang and Berg, 2006). Finally, we demonstrate the impact of consolidation on clay erosion threshold, which can be explained by clay microstructure as well.

2 Measurements and Experimental Setup

We used a grid-stirred reactor (grid-turbulence tank) to recreate a range of shear stress and turbulent kinetic energy. The reactor consists of a 50x50x50 cm clear plexiglass tank and a grid driven by a reciprocating electric motor (Figure 1). The grid rests at 21 cm in average distance from the bed. The grid has a stroke length of 14 cm and can oscillate vertically at a maximum frequency of 100 rpms. This tank has been used for studies of fine sediment entrainment and sediment-gas transfer (e.g., Valsaraj, et al., 1997; Orlins and Gulliver, 2003).

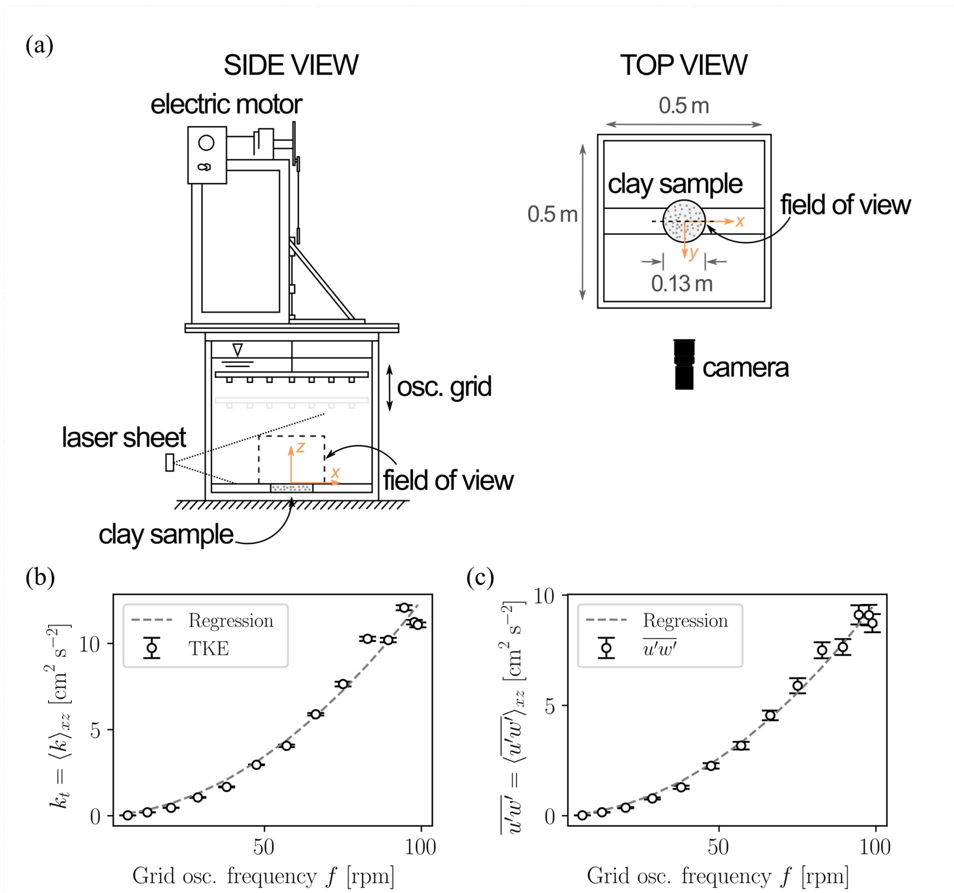

Figure 1. Experimental setup. (A) A schematic of the oscillating tank and the particle image velocimetry arrangement. Clay sample was placed in the middle of the tank at the bottom. Subfigures (B) and (C) show the distribution of spatial-averaged turbulent kinetic energy ($k_t = 0.001f^2 + 0.012f$) and Reynolds stress $\overline{u'w'}$ ($\overline{u'w'} = 0.001f^2 + 0.07f$) as a function of grid oscillation frequency f.

We used the synthetic smectite clay laponite (Laponite-RD, BYK Additives and Instruments, 2013) to represent cohesive smectite clay. Laponite is a phyllosilicate clay formed by layers of octahedrally coordinated magnesium oxide in between two parallel layers of tetrahedrally coordinated silica (Ruzicka and Zaccarelli, 2011). Laponite resembles naturally occurring clay hectorite (Ruzicka and Zaccarelli, 2011) and has been used in colloidal and transparent-soil geotechnical studies (Jeong et al., 2010; Chini et al., 2015; Wallace and Rutherford, 2015). Its rheological characteristics in response to water salinity and consolidation has been identified (Tanaka et al., 2004). Laponite becomes clear when it hydrates allowing us to visualize the clay surface to track its erosion. We hydrated laponite with an aqueous rhodamine solution at 2.72 mg L^{-1} to produce fluorescent clay. Rhodamine (Rhodamine-WT, Thermo Fisher Scientific, 2011) is a fluorescent dye in aqueous solution that emits yellow-orange wavelength (557 nm) when excited with a 532 nm wavelength light (Smart and Laidlaw, 1977).

A Particle Image Velocimetry (PIV) system was used to measure flow velocity inside the tank . It consists of a continuous 2A 532 nm wavelength laser and a 5MP Blackfly S USB3 FLIR camera. We captured instantaneous two-component two-dimensional velocity fields in a 14.4x2.9 cm Field of View (FOV) near the bed. Spinnaker software (FLIR Systems, Inc.) works as the interface to set up the camera parameters and collect images. Over a range of sampling rates between 10 Hz and 175 Hz, we obtained spatial and temporal resolution in the order of 1 mm and 5 ms, processing the PIV images in PIVLab (Thielicke and Sonntag, 2021).

To identify the erosion threshold of clay, we visually tracked the erosion of clay samples through the PIV system and the fluorescent dye rhodamine. We illuminated the fluorescent clay with the PIV laser during the erosion tests, while capturing images of the clay sample with the FLIR camera through a 550 nm center wavelength lens filter. This is a comparable approach to the production and use of inexpensive fluorescent PIV particles (Pedocchi et al., 2008). Erosion test consisted of stepwise increments of grid's oscillation frequency inside the tank while tracking changes in the clay surface. Specifically, clay samples were exposed to grid-turbulence during 5-minutes per oscillation frequency increment. We captured time series imaging of the clay surface at sample frequency of 1 Hz. Monochromatic imaging of the surface provided a baseline for the undisturbed sample image intensity for erosion threshold identification (Figure S1A).

In addition to PIV measurements, a Nikon-C2+ confocal laser scanning microscope (CLSM) with 10X and 20X objectives was used to visualize the microstructure of clay. Specifically, we selected some clay samples and visualized their microstructures through 2048x2048-pixel images with 0.31 μm/pixel resolution. The laser used for CLSM has an emission wavelength of 525 nm and an excitation wavelength of 488 nm.

To assess the impact of salinity and consolidation on the erosion threshold, we conducted clay erosion experiments using five water salinities, from 0.15 to 3.02 ppt (parts-per-thousand). The highest salinity corresponds to most consequential salinity conditions to cohesive sediment erosion in coastal settings (Krone, 1962; Parchure and Mehta, 1985). We prepared each saline solution with table salt (NaCl) and tap water in a mixing tank and measured salinity using a conductivity probe (PC Premium Multi-Parameter Tester, Apera Instruments). We prepared the clay dispersions by filling a 13 cm diameter petri dish with the saline solution and pouring laponite evenly on the surface of the saline solution through a U.S. standard sieve No 60 (sieve opening 0.25 mm). For consolidated samples, we allow the clay to settle and aggregate for 17 hours before testing, whereas unconsolidated samples are tested immediately.

3 Data Analysis

We characterized near-bed hydrodynamics of the turbulence tank as a function of grid's oscillation frequency. Here, longitudinal, lateral, and vertical coordinates are x, y, and z, respectively, with origin at the center of the tank (Figure 1). Their respective flow velocity components are u, v, and w. From the PIV measurements, we estimated flow statistics including turbulent kinetic energy ($k_t = 0.5(\overline{u'} + \overline{v'} + \overline{w'})$), and Reynolds stresses ($\overline{u'w'}$). Longitudinal and lateral velocity components (u and v, respectively) are equivalent, $u \sim v$, because of axial symmetry of the tank's hydrodynamics around the vertical axis z. Axial symmetry comes from the turbulence homogeneity in the longitudinal and lateral x-$y$plane created by a vertical oscillating grid (Hopfinger and Toly, 1976; De Silva and Fernando, 1992).

Turbulence is uniformly distributed over the near-bed region across x-y plane where turbulent kinetic energy k_t and Reynolds stresses $\overline{u'w'}$ reach maximum local in the order of 10 cm^2 s^{-2} (Figure S2). It suggests that the turbulent fluctuations are well distributed over the surface of the clay sample. The k_t is also uniformly distributed vertically over the Field of View's height (2.9 cm, Figure S2). In contrast, Reynolds stress $\overline{u'w'}$ profiles display a decreasing behavior towards the bed. We used vertically averaged turbulent kinetic energy over the FOV's height the as a near-bed hydrodynamic parameter to quantify the turbulent erosive capacity (Figure S3). Reynolds stress $\overline{u'w'}$ becomes a turbulent parameter directly associated with an equivalent estimation of bed shear stress ($\tau_b = \rho\overline{u'w'}$, where ρ is water density, Pope et al., 2006). A quadratic function fits well with the vertically averaged turbulent kinetic energy and Reynolds stress $\overline{u'w'}$ over the full range of grid's frequency oscillations (0 to 100 rpm, Figure 1).

Table 1. Summary of all experimental cases tested in this work. Consolidated samples are allowed to consolidate over a period of 17 hours, while unconsolidated cases tested immediately.

Salinity [ppt]	**Ionic strength [M]**	**Consolidated [Number of replicates]**	**Unconsolidated [Number of replicates]**
0.15	2.57×10^{-3}	4	4
0.26	4.45×10^{-3}	4	4
0.77	1.32×10^{-2}	6	4
1.52	2.60×10^{-2}	3	4
3.04	5.20×10^{-2}	5	4

To identify the threshold of erosion, we tracked changes of the clay surface using the mean Structural Similarity method (Wang et al, 2004). This method uses luminance, contrast, and structural comparison between images to measure a degree of similarity. We calculated MSSIM series between a baseline undisturbed 5-minute averaged image and the running 5-minute averaged image at the end of each grid frequency increment. We established erosion threshold as the hydrodynamic condition where the MSSIM series loses 10-percent of structural similarity. Therefore, we linearly interpolated to estimate the 10-percent crossing value of the MSSIM index in terms of turbulent kinetic energy, Reynolds number, and bed shear stress. In addition, each salinity and consolidation combination were replicated between three and four times (Table 1).

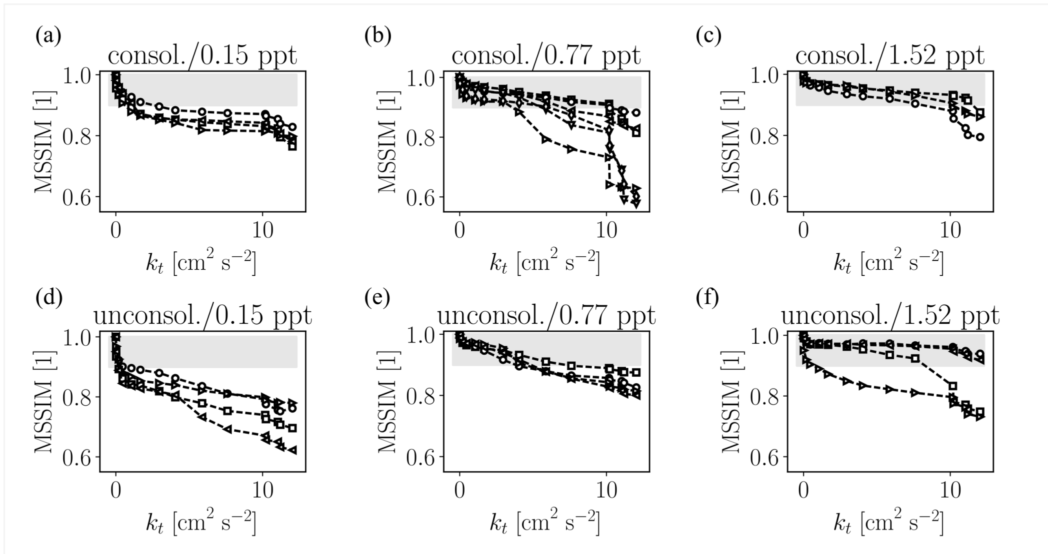

Figure 2. Identification of the threshold k_t to erode clay. Series of Mean Structural-Similarity Index (MSSIM) for three salinity conditions: 0.15 ppt (A, D), 0.77 ppt (B, E), and 1.52 ppt (C, F). A to C are for consolidated conditions, while D to F for unconsolidated cases. Gray area within the subplots marks the 10-percent reduction of structural similarity of the sample with respect to the initial condition.

4 Results

First, we identified the critical turbulent kinetic energy, $k_{t,\,crit}$, and bed shear stress, $\tau_{b,crit}$, to erode laponite clay under different salinity and consolidation conditions. The change in clay surface's structural similarity by 10-percent, using MSSIM method, was used to identify $k_{t,\,crit}$ (gray area indicates 10-percent, Figure 2). Note that we observed surface and mass erosion from clay over a range of salinities (Winterwerp et al., 2022). During our experiments, both erosion forms occurred across both clay states (Figure S4). However, the erosion threshold takes place within the early surface erosion mode. Our results show that $k_{t,\,crit}$ and τ_{crit} increases with salinity for concentrations less than 1.52 ppt for both consolidated and nonconsolidated cases (Figure 3A), indicating that clay is more easily eroded at lower values of salinity regardless of consolidation at ionic strength less than 2.60×10^{-2} M. In contrast, at ionic strength higher than 2.60×10^{-2} M, $k_{t,\,crit}$ and $\tau_{b,crit}$ decrease as salinity increase. The maximum $k_{t,\,crit}$ and critical bed shear stress, $\tau_{b,crit}$, for consolidated cases are 9.9 cm^2 s^{-2} and 0.76 N m^{-2}, respectively, which are over 11 times larger than the lowest values 0.87 cm^2 s^{-2} and 0.07 N m^{-2}, suggesting that salinity play a crucial role in cohesive clay transport.

Second, we show that the non-monotonic dependency of $k_{t,\,crit}$ and $\tau_{b,\,crit}$ on salinity is related to a change in the phase or microstructure of clay with increasing ionic strength. Specifically, Tanaka et al. (2004) suggest that laponite clay forms gel, which is a network of cross-lined particles, when ionic strength is less than 1.06×10^{-2} M which is equivalent to 1.03 ppt (gray area in Figure 3) and forms separated microaggregates when salinity is higher than 1.03 ppt. To test whether the non-monotonic dependency of $k_{t,\,crit}$ and $\tau_{b,crit}$ on salinity is due to differences in clay status, i.e., gel versus phase separation, we visualized the microstructure of clay using a confocal laser scanning microscope. As shown in the four inserts of Figure 3, in the salinity range of clay gel (salinity <1.52 ppt), the clay looks uniform, indicating formation of a uniform cross-linked material. In contrast, in the salinity range of phase separation (salinity >1.52 ppt), the clay forms many separated micro-aggregates, confirming the formation of phase-separated structures. The difference in clay microstructures at low and high salinity range and the non-monotonic dependency of $k_{t,\,crit}$ and $\tau_{b,crit}$ on salinity suggest that clay microstructures play a critical role on the erosion of clay. The formation of gel increases the critical $k_{t,\,crit}$ and $\tau_{b,crit}$ required to erode clay. At high salinity range, $k_{t,\,crit}$ and $\tau_{\mathrm{b,crit}}$ decrease with salinity because clay no longer form gels. Our results indicate that salinity controls erosion threshold clay by controlling the microscale interactions among clay.

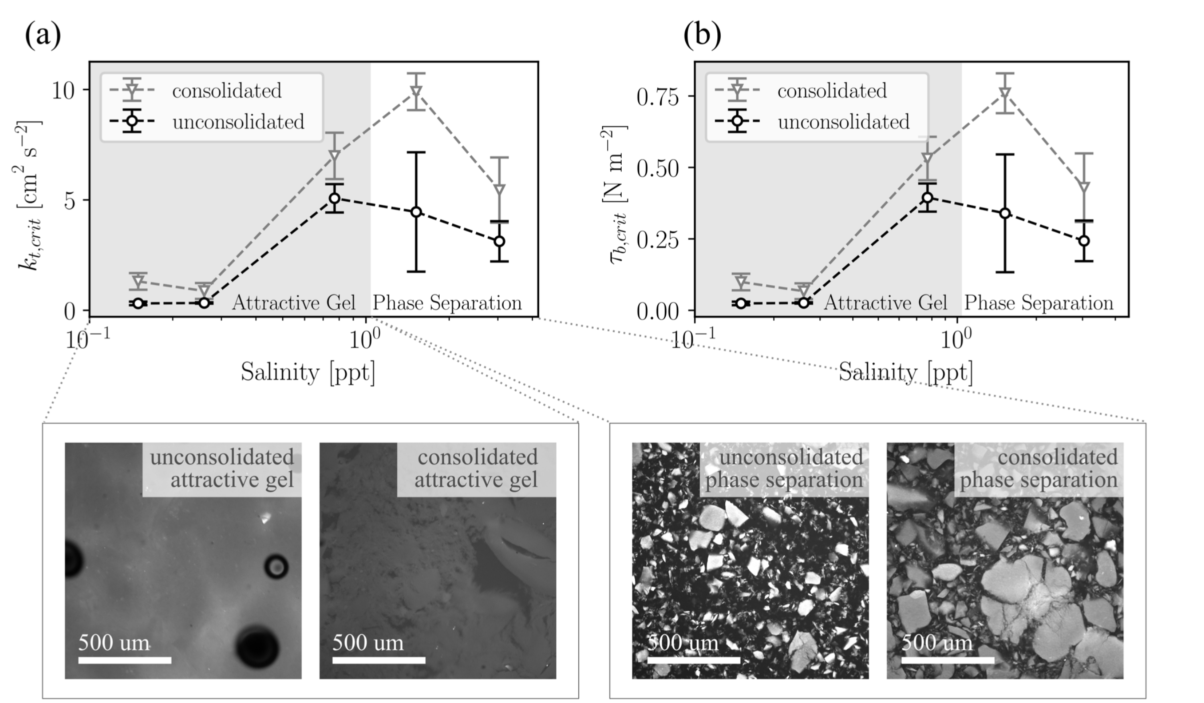

Figure 3. The critical turbulent kinetic energy $k_{t,\,crit}$ (A) and critical bed shear stress $\tau_{b,crit}$ (B) to erode consolidated and unconsolidated clay at different salinities. Gray area indicates range of salinity when laponite forms gel and the white area indicates the range of salinity when laponite form phase-separated aggregates (Tanaka et al., 2004). The four images below the figures are confocal microscopic images of clay samples at different salinity range and consolidation conditions. The salinity for attractive gel state and phase-separation state are 0.15 ppt and 3.02 ppt, respectively. The black circles on the left-most confocal images are gas bubbles.

In addition to salinity, we investigated the impacts of consolidation on $k_{t,\,crit}$ and $\tau_{b,\,crit}$. We compared the critical condition to erode non-consolidated clay with the condition to erode clay consolidation for 17 hours (Figure 3). Our results show that consolidation increased the threshold for erosion for all salinity conditions considered here. The maximum $k_{t,\,crit}$ and $\tau_{b,crit}$ for nonconsolidated cases are 5.07 cm^2 s^{-2} and 0.39 N m^{-2}, respectively. They are over 1.9 times less than their consolidated maximum values, indicating consolidation plays an important yet secondary role (compared with salinity) on cohesive clay transport. The increase in $k_{t,\,crit}$ and $\tau_{b,crit}$ due to consolidation can also be explained by clay microstructures. First, for clay in gelatinous states, the amount of micro-size gas bubbles reduced after consolidation (insets in

Figure 3), which likely contribute to the increase in density and erosion threshold. Second, for clay in phase separated state, the size of clay micro-aggregates increased after consolidation, which explains the increase in threshold for erosion due to consolidation at the high salinity range (salinity >1.52 ppt).

5 Discussions

5.1 The effect of gelation on erosion threshold.

First, we attribute the non-monotonic dependency of erosion threshold on water salinity to clay gelation. Increasing salinity increases erosion threshold up to salinities 0.77 and 1.52 ppt for the unconsolidated clay and consolidated conditions, respectively (Figure 3). Then, erosion threshold decreases with salinity for higher salt concentrations. This inflection point coincides with the clay transition from attractive gel to phase-separation state 1.03 ppt observed in Tanaka et al., (2004). Aggregated clay takes different rheological states as a function of salinity, such as flocculated clay aggregates, “fluid mud”, and gelling clay (Winterwerp et al., 2022). Under low salinity concentrations, clay may resemble a gel constitution effectively increasing the flow energy required to erode it. Higher salinity leads to more discrete and loose aggregates under the phase-separation state. This state makes the aggregates prompt to entrainment.

5.2 The effect of consolidation and partial aggregation on erosion threshold.

Second, we confirm that consolidation increases the erosion threshold of clay. Specifically, we observed that erosion threshold is higher for all consolidated cases than in unconsolidated conditions (Figure 3). Clay consolidation strengthens the inter-aggregate bonding by pushing out porous water and allowing longer flocculation (Winterwerp et al., 2022). Studies have observed an overall increase in mud resistance to erosion associated to higher sediment density due to consolidation (e.g., Maa and Mehta, 1987; Mitchener and Torfs, 1996. In addition, the consolidation process increases the clay density (Mehta et al., 1989). Therefore, clay consolidation takes place along with increasing aggregation of the sample.

5.3 Implications for coastal environments.

Finally, our results have shown that salinity and consolidation, which determines clay gelation state, control the erosion threshold of clay. The underestimation of fine sediment transport in riverine environments tends to overlook the effect of flocculation and floc size development (Lamb, et al., 2020). In analogy, gelation, and erosion mode of fine cohesive material can be overlooked, potentially leading to uncertainties of the sediment transport capacity in coastal environments. The mode of erosion (surface and detachment) defines the size of entrained floc aggregates at different instances (Winterwerp et al., 2012). It means that a single characteristic floc size may likely misrepresent entrainment and deposition rates. These findings have implications for modeling sediment transport in environments subject to salinity gradient and history of consolidation. Current erosion models define a single erosion threshold value based on in-situ or laboratory testing (Winterwerp et al., 2012). However, this approach needs to be adapted to account for changes in erosion onset under different salinity conditions. The non-monotonic behavior of erosion threshold with respect to turbulent kinetic energy and bed shear stress suggests we should revisit our current relations for erosion threshold for coastal environments.

5 Conclusions

Here we estimate the erosion threshold of smectite clay as a function of salinity and consolidation using fluorescence-based visualization technology, including Particle Image Velocimetry and Confocal Laser Scanning Microscopy. A new method based on series of structural-similarity index was used to track the erosion of a fluorescently-labelled transparent smectite clay, laponite. Our results show that salinity can lead to an order of magnitude difference in the critical shear stress to erode clay and consolidation can increase the critical shear stress by almost two folds. Moreover, we demonstrate that erosion threshold follows a non-monotonic relation with water salinity due to the gelation state of clay, where the cohesive sediment is increasingly more resistant to erosion under a gel phase as a function of salinity. Higher concentration of dissolved salt leads to a clay state change to phase-separation, where erosion threshold decreases with increasing salinity. In addition, consolidation enhances the shear strength of the cohesive sediment regardless of clay state. Furthermore, our confocal laser scanning microscopic images of clay samples demonstrate that the monotonic dependency of erosion threshold on water salinity and the increase in erosion threshold with consolidation are reflected in the changes in the microstructures of clay. These findings highlight the critical role of the microstructures or gelation state of clay in cohesive sediment transport under different salinity and consolidation conditions. Our results highlight the need to incorporate the microstructure or gelation state of clay, in addition to salinity and consolidation, into preditions of cohesive sediment erosion in changing salinity environments.

Acknowledgements

This study was supported by JQY’s startup funds from the University of Minnesota Twin Cities and National Science Foundation grant EAR 2150796. The authors would like to thank Benjamin Erickson and Jeffrey Marr for help with the experimental setup.

Open Research

The raw images of the clay surface during the erosion experiments, processed flow measurements, and series of structural-similarity index to identify erosion threshold have been deposited in The Data Repository for University of Minnesota (https://conservancy.umn.edu/handle/11299/227649) .

References

Adam, P. (2019). Salt marsh restoration. In *Coastal wetlands* (pp. 817-861). Elsevier.

Berlamont, J., Ockenden, M., Toorman, E., & Winterwerp, J. (1993). The characterisation of cohesive sediment properties. *Coastal Engineering*, *21*(1-3), 105-128.

BYK Additives and Instruments, LAPONITE RD: The Clear Leader, LAPONITE RD Datasheet, Oct. 2013.

Chini, C. M., Wallace, J. F., Rutherford, C. J., & Peschel, J. M. (2015). Shearing failure visualization via particle tracking in soft clay using a transparent soil. *Geotechnical Testing Journal*, *38*(5), 708-724.

De Jonge, V. N. (1988). The abiotic environment. In *Tidal flat estuaries* (pp. 14-27). Springer, Berlin, Heidelberg.

De Silva, I. P. D., & Fernando, H. J. S. (1992). Some aspects of mixing in a stratified turbulent patch. *Journal of Fluid Mechanics*, *240*, 601-625.

Forsberg, P. L., Skinnebach, K. H., Becker, M., Ernstsen, V. B., Kroon, A., & Andersen, T. J. (2018). The influence of aggregation on cohesive sediment erosion and settling. *Continental Shelf Research*, *171*, 52-62.

Gao, S. (2019). Geomorphology and sedimentology of tidal flats. In *Coastal Wetlands* (pp. 359-381). Elsevier.

Grabowski, R. C., Droppo, I. G., & Wharton, G. (2011). Erodibility of cohesive sediment: The importance of sediment properties. *Earth-Science Reviews*, *105*(3-4), 101-120.

Guillou, S., Thiebot, J., Chauchat, J., Verjus, R., Besq, A., Nguyen, D. H., & Pouv, K. S. (2011). The filling dynamics of an estuary: from the process to the modelling.

Haight, C., Larson, M., Swadek, R. K., & Hartig, E. K. (2019). Toward a salt marsh management plan for New York City: recommendations for strategic restoration and protection. In *Coastal Wetlands* (pp. 997-1022). Elsevier.

Hedström, M., Hansen, E. E., & Nilsson, U. (2016). Montmorillonite phase behaviour. *Clay Technology AB*.

Hopfinger, E. J., & Toly, J. A. (1976). Spatially decaying turbulence and its relation to mixing across density interfaces. *Journal of fluid mechanics*, *78*(1), 155-175.

Huang, A. Y., & Berg, J. C. (2006). High-salt stabilization of Laponite clay particles. *Journal of colloid and interface science*, *296*(1), 159-164.

Jeong, S. W., Locat, J., Leroueil, S., & Malet, J. P. (2010). Rheological properties of fine-grained sediment: the roles of texture and mineralogy. *Canadian Geotechnical Journal*, *47*(10), 1085-1100.

Kennish, M. J. (2001). Coastal salt marsh systems in the US: a review of anthropogenic impacts. *Journal of Coastal Research*, 731-748.

Krone, R. B. (1962). Flume studies of transport of sediment in estrarial shoaling processes. *Final Report, Hydr. Engr. and Samitary Engr. Res. Lab., Univ. of California*.

Lamb, M. P., de Leeuw, J., Fischer, W. W., Moodie, A. J., Venditti, J. G., Nittrouer, J. A., ... & Parker, G. (2020). Mud in rivers transported as flocculated and suspended bed material. *Nature Geoscience*, *13*(8), 566-570.

Lick, W. & McNeil, J., (2001). Effects of sediment bulk properties on erosion rates. *Science of the Total Environment*, *266*(1-3), pp.41-48.

Maa, P. Y., & Mehta, A. J. (1987). Mud erosion by waves: a laboratory study. *Continental Shelf Research*, *7*(11-12), 1269-1284.

Mehta, A. J. (1986). Characterization of cohesive sediment properties and transport processes in estuaries. In *Estuarine cohesive sediment dynamics* (pp. 290-325). Springer, New York, NY.

Mehta, A. J., Hayter, E. J., Parker, W. R., Krone, R. B., & Teeter, A. M. (1989). Cohesive sediment transport. I: Process description. *Journal of Hydraulic Engineering*, *115*(8), 1076-1093.

Mitchener, H., & Torfs, H. (1996). Erosion of mud/sand mixtures. *Coastal engineering*, *29*(1-2), 1-25.

Mongondry, P., Tassin, J. F., & Nicolai, T. (2005). Revised state diagram of Laponite dispersions. *Journal of Colloid and Interface Science*, *283*(2), 397-405.

Nicholson, J., & O'Connor, B. A. (1986). Cohesive sediment transport model. *Journal of Hydraulic Engineering*, *112*(7), 621-640.

Orlins, J. J., & Gulliver, J. S. (2003). Turbulence quantification and sediment resuspension in an oscillating grid chamber. *Experiments in Fluids*, *34*(6), 662-677.

Parchure, T. M., & Mehta, A. J. (1985). Erosion of soft cohesive sediment deposits. *Journal of hydraulic engineering*, *111*(10), 1308-1326.

Partheniades, E. (1986). A fundamental framework for cohesive sediment dynamics. In *Estuarine cohesive sediment dynamics* (pp. 219-250). Springer, New York, NY.

Pieterse, A., Puleo, J. A., McKenna, T. E., & Figlus, J. (2017). In situ measurements of shear stress, erosion and deposition in man-made tidal channels within a tidal saltmarsh. *Estuarine, Coastal and Shelf Science*, *192*, 29-41.

Pedocchi, F., Martin, J. E., & García, M. H. (2008). Inexpensive fluorescent particles for large-scale experiments using particle image velocimetry. *Experiments in Fluids*, *45*(1), 183-186.

Pedocchi, F., & García, M. H. (2012). Acoustic measurement of suspended sediment concentration profiles in an oscillatory boundary layer. *Continental Shelf Research*, *46*, 87-95.

Pope, N. D., Widdows, J., & Brinsley, M. D. (2006). Estimation of bed shear stress using the turbulent kinetic energy approach—A comparison of annular flume and field data. *Continental Shelf Research*, *26*(8), 959-970.

Sartor, L. R., Graham, R. C., Ying, S. C., Andrade, G. R., Montes, C. R., & Ferreira, T. O. (2019). Are hypersaline tidal flat soils potential silicon sinks in coastal wetlands?. *Geoderma*, *337*, 215-224.

Smart, P. L., & Laidlaw, I. M. S. (1977). An evaluation of some fluorescent dyes for water tracing. *Water resources research*, *13*(1), 15-33.

Ruzicka, B., & Zaccarelli, E. (2011). A fresh look at the Laponite phase diagram. *Soft Matter*, *7*(4), 1268-1286.

Tanaka, H., Meunier, J., & Bonn, D. (2004). Nonergodic states of charged colloidal suspensions: Repulsive and attractive glasses and gels. *Physical Review E*, *69*(3), 031404.

Thielicke, W., & Sonntag, R. (2021). Particle Image Velocimetry for MATLAB: Accuracy and enhanced algorithms in PIVlab. *Journal of Open Research Software*, *9*(1).

Thermo Fisher Scientific, Rhodamine WT, 20% solution in water, RHODAMINE-WT Safety Datasheet, Sep. 2011.

Thompson, D. W., & Butterworth, J. T. (1992). The nature of laponite and its aqueous dispersions. *Journal of Colloid and Interface Science*, *151*(1), 236-243.

Valsaraj, K. T., Ravikrishna, R., Orlins, J. J., Smith, J. S., Gulliver, J. S., Reible, D. D., & Thibodeaux, L. J. (1997). Sediment-to-air mass transfer of semi-volatile contaminants due to sediment resuspension in water. *Advances in Environmental Research*, *1*(2), 145-156.

Wallace, J. F., & Rutherford, C. J. (2015). Geotechnical properties of LAPONITE RD®. *Geotechnical Testing Journal*, *38*(5), 574-587.

Wang, Z., Bovik, A. C., Sheikh, H. R., & Simoncelli, E. P. (2004). Image quality assessment: from error visibility to structural similarity. *IEEE transactions on image processing*, *13*(4), 600-612.

Winterwerp, J. C., Van Kesteren, W. G. M., Van Prooijen, B., & Jacobs, W. (2012). A conceptual framework for shear flow–induced erosion of soft cohesive sediment beds. *Journal of Geophysical Research: Oceans*, *117*(C10).

Winterwerp, J. C., Erftemeijer, P. L. A., Suryadiputra, N., Van Eijk, P., & Zhang, L. (2013). Defining eco-morphodynamic requirements for rehabilitating eroding mangrove-mud coasts. *Wetlands*, *33*(3), 515-526.
Winterwerp, J. C., Van Kessel, T., van Maren, D. S., & Van Prooijen, B. C. (2022). *Fine Sediment in Open Water: From Fundamentals to Modeling*.
Yuan, J., Zheng, B., Wang, R., Zhang, M., & Yu, G. (2022). Chloride salt sorption flux of cohesive sediment beds with different degrees of fluidization in quiescent water. *Applied Ocean Research*, *118*, 102933.
Zhang, M., & Yu, G. (2017). Critical conditions of incipient motion of cohesive sediments. *Water Resources Research*, *53*(9), 7798-7815.s

AGU PUBLICATIONS

Geophysical Research Letters

Supporting Information for

Impacts of Salinity and Consolidation on the Microstructure and Erosion Threshold of Cohesive Sediment

Jorge E. San Juan[1], William G. Wei[1], and Judy Q. Yang[1]

[1] St. Anthony Falls Laboratory, Department of Civil, Environmental, and Geo-Engineering, University of Minnesota Twin Cities, MN, USA.

Contents of this file

Introduction

Text S1 provides information on the post-processing of the clay surface's images and estimation of structural similarity-index. Figure S1 displays the fluorescent surface of laponite in the tank and the time series of normalized average intensity of clay surfaces. Figure S2 shows a 2D turbulent kinetic energy k_t and 2D Reynolds stress $\overline{u'w'}$ fields as a sample of hydrodynamic characterization of the turbulence. Figure S3 shows turbulent kinetic energy k_t and Reynolds stress $\overline{u'w'}$ vertical profiles. Figure S4 illustrates the surface and mass erosion modes through the luminance difference between the two raw images at the beginning and end of the erosion tests.

Text S1. Image post-processing and structural similarity

For each erosion test, we identified and cropped the subset area within the field of view's instantaneous image where the clay sample's surface was. Cropped images enabled us to isolate the changes of the clay surface within the image (Figure Figure S1A). Because the images are capture in monochromatic format, we initially image-averaged the intensities from each instantaneous cropped image. Normalizing the averaged intensity time series by the averaged intensity at the last measurement, we noticed the time evolution of the image intensities due to changes in the eroded clay surface (Figure Figure S1B). However, intensity alone does not show a clear picture for the erosion threshold of fluorescently labelled laponite. Averaging the cropped images taken during each 5-minute grid oscillation frequency, we implemented structural similarity to quantify for changes in the eroded clay surface.

The structural-similarity index is a robust image quality metric to quantify how much two images are similar to each other (Wang et al., 2004). This method was developed to overcome ambiguities in mean-squared error methods applied to image processing for image comparison. Given two non-negative image signals A and B, structural similarity S uses luminance, contrast, and structure parameters (see Eq. 1) as a combination of mean intensity (μ_a), standard deviation (σ_a), and correlation coefficient (σ_{ab}); where subindices a and b indicate the image signal A and B, respectively. Eq. 2, Eq. 3, and Eq. 4 show formulations for estimating luminance comparison, contrast comparison, and structure comparison, respectively. Wang et al. (2004) proposes to Structural-Similarity index, SSIM, as in Eq. 5. Here, $C_1 = (K_1 L)^2$, $C_2 = (K_2 L)^2$, and $C_3 = C_2/2$ are constants. Parameters L is the dynamic range of the pixel values (255 for 8-bit grayscale images), and K_1 and K_2 are small constants (0.01 and 0.03, respectively).

$$S(A,B) = f(l(A,B), c(A,B), s(A,B)) \qquad \text{Eq. 1}$$

$$l(A,B) = \frac{2\mu_a\mu_b + C_1}{{\mu_a}^2 + {\mu_b}^2 + C_1} \qquad \text{Eq. 2}$$

$$c(A,B) = \frac{2\sigma_a\sigma_b + C_2}{{\sigma_a}^2 + {\sigma_b}^2 + C_2} \qquad \text{Eq. 3}$$

$$s(A,B) = \frac{\sigma_{ab} + C_3}{\sigma_a\sigma_b + C_3} \qquad \text{Eq. 4}$$

$$SSIM(A,B) = \frac{(2\mu_a\mu_a + C_1)(2\sigma_{ab} + C_2)}{({\mu_a}^2 + {\mu_b}^2 + C_1)({\sigma_a}^2 + {\sigma_b}^2 + C_2)} \qquad \text{Eq. 5}$$

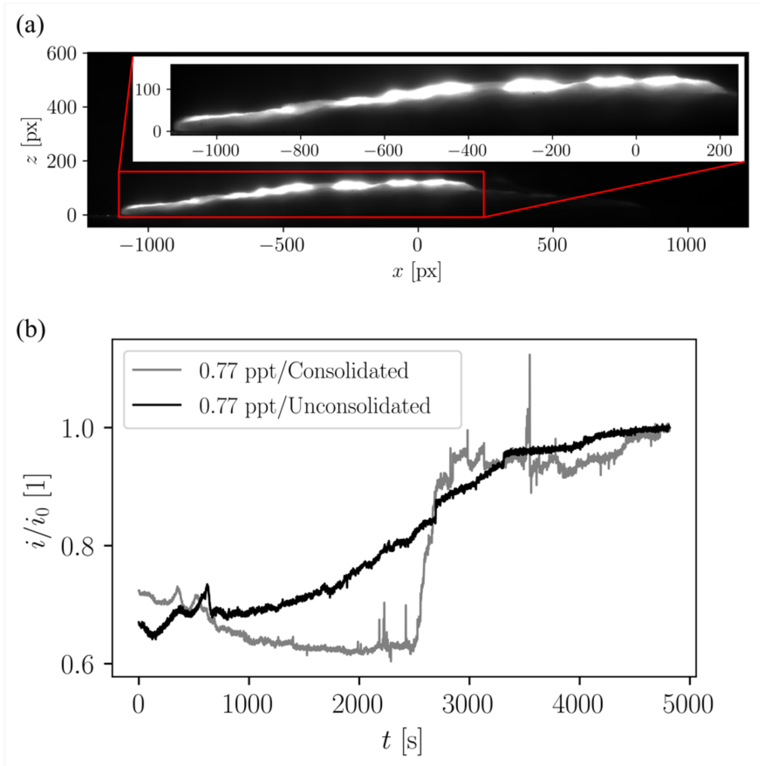

Figure S1. (A) Image showing the illuminated fluorescent surface (white color) of laponite in the tank. The clay was consolidated for 17 hours at salinity 0.77 ppt. (B) Time evolution of normalized average intensity of clay surfaces for samples at salinity 0.77 ppt under consolidated and unconsolidated conditions. Variable i is the instantaneous spatial-averaged image intensity and i_0 is the image-averaged intensity at the end of the test.

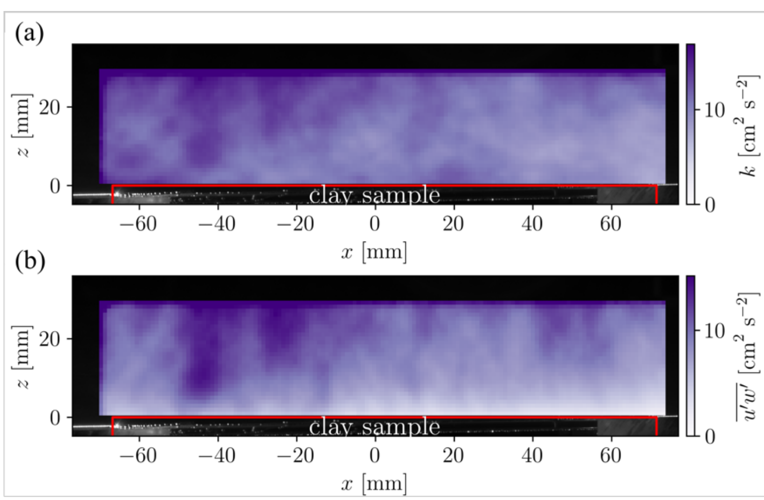

Figure S2. (A) 2D turbulent kinetic energy field k and (B) 2D Reynolds stress field $\overline{u'w'}$ at 98.87 rpm. Red solid line indicates the location of the clay sample.

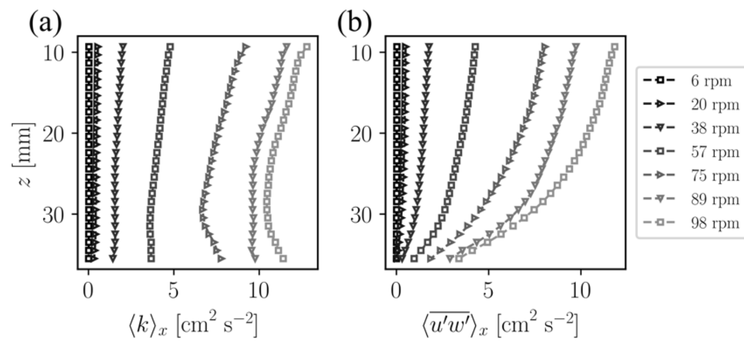

Figure S3. (A) Longitudinally (along x-direction) averaged turbulent kinetic energy vertical profile and (B) longitudinally averaged Reynolds stress $\overline{u'w'}$ vertical profile for a selection of grid oscillation frequencies.

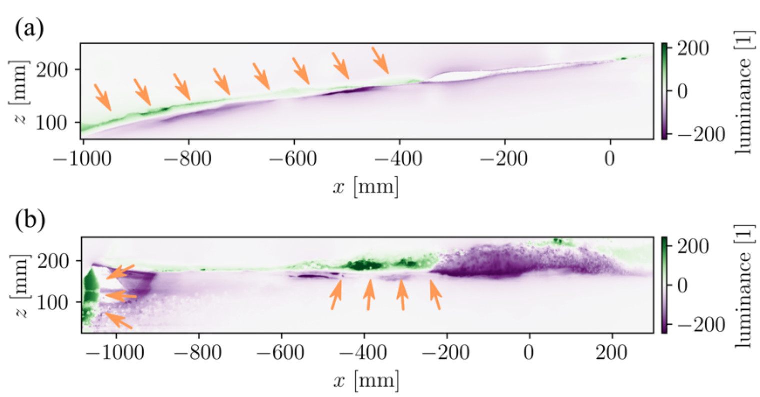

Figure S4. Highlights of elevation change due to erosion as the luminance difference between the two raw images at the beginning and end of the erosion tests. (A) Surface erosion of a consolidated clay sample at salinity 1.52 ppt. Arrows indicate the relatively uniformly distributed surface erosion rather than localized erosion. (B) Mass erosion in a clay sample at salinity 0.26 ppt. Arrows indicate the localized detachment erosion.